arXiv:2301.03519v1 [astro-ph.SR] 9 Jan 2023

Evolution of elemental abundances in hot active region cores from Chandrayaan-2 XSM observations

Biswajit Mondal,[1,2] Santosh V. Vadawale,[1] Giulio Del Zanna,[3] N. P. S. Mithun,[1] Aveek Sarkar,[1]
Helen E. Mason,[3] P. Janardhan,[1] and Anil Bhardwaj[1]

[1] Physical Research Laboratory, Navrangpura, Ahmedabad, Gujarat-380 009, India
[2] Indian Institute of Technology Gandhinagar, Palaj, Gandhinagar, Gujarat-382 355, India
[3] DAMTP, Centre for Mathematical Sciences, University of Cambridge, Wilberforce Road, Cambridge CB3 0WA, UK

ABSTRACT

The First Ionization Potential (FIP) bias, whereby elemental abundances for low FIP elements in different coronal structures vary from their photospheric values and may also vary with time, has been widely studied. In order to study the temporal variation, and to understand the physical mechanisms giving rise to the FIP bias, we have investigated the hot cores of three ARs using disk-integrated soft X-ray spectroscopic observation with the Solar X-ray Monitor (XSM) onboard Chandrayaan-2. Observations for periods when only one AR was present on the solar disk were used so as to ensure that the AR was the principal contributor to the total X-ray intensity. The average values of temperature and EM were ∼3 MK and 3×10^{46} cm^{-3} respectively. Regardless of the age and activity of the AR, the elemental abundances of the low FIP elements, Al, Mg, and Si were consistently higher than their photospheric values. The average FIP bias for Mg and Si was ∼3, whereas the FIP bias for the mid-FIP element, S, was ∼1.5. However, the FIP bias for the lowest FIP element, Al, was observed to be higher than 3, which, if real, suggests a dependence of the FIP bias of low FIP elements on their FIP value. Another major result from our analysis is that the FIP bias of these elements is established in within ∼10 hours of emergence of the AR and then remains almost constant throughout its lifetime.

Keywords: Solar X-ray corona, Solar abundances, FIP bias, FIP effect, Active Region

1. INTRODUCTION

The earlier study of the Sun as a star by Pottasch (1963) revealed that solar coronal abundances are different from those of the photosphere. The differences are correlated to the First Ionization Potential (FIP) of the element, in the sense that the abundance ratio of a low-FIP (less than 10 eV) element versus that of a high-FIP element is higher in the corona. A measure of the difference is the so called FIP bias, i.e. the ratio between the coronal and the photospheric abundance of an element.

In most of the available literature, the FIP bias has been (and still is) estimated by measuring the relative abundances between elements, and not relative to hydrogen. This is due to the fact that abundance measurements with respect to Hydrogen in the low corona, and on-disk is non-trivial, due to the lack of H-emission lines at a few million Kelvin. Hence, whether it is the low-FIP elements that have an increased abundance or the high-FIP elements that have a reduced one (compared to their photospheric values) has been a subject of continued debate.

Further, it has become clear that different solar structures have different FIP biases. There are also indications that the FIP bias depends on the temperature of the plasma. For a long time, it has been widely accepted that coronal abundances in active regions increase with time. We refer the reader to the recent reviews by Laming (2015); Del Zanna and Mason (2018) for more details. We also provide in the following section a brief summary of available measurements related to active regions.

Knowledge of the elemental abundances in different atmospheric layers of the Sun is a topic of great interest to the solar physics community mainly due to the following two reasons. The first is that they provide, in principle, a way to link the solar source regions to the various components of the solar wind. In fact, elemental abundance variations are also clearly observed in-situ.

Corresponding author: Biswajit Mondal
biswajit70mondal94@gmail.com, biswajitm@prl.res.in

The slow-speed solar wind has a high FIP bias similar to that measured in AR core loops, 3MK, whereas the high-speed wind has a near unit FIP bias, similar to that of coronal holes (see, e.g., Brooks et al. 2015; Gloeckler and Geiss 1989; Feldman et al. 1998; Bochsler 2007; Brooks and Warren 2011).

The second reason is that studying abundance variations might contribute to a better understanding of the physical processes at play in the solar corona. In fact, we know that the FIP bias is closely related to the magnetic field activity of the Sun (see, e.g. Feldman and Widing 2002; Brooks et al. 2017; Baker et al. 2018). The Ponderomotive force model (Laming 2004, 2009, 2012, 2017) is now widely accepted, as it is able to reproduce the main characteristics of the FIP effect, as measured in-situ and remotely. According to this model, the separation of ions from neutral atoms within closed loops in an upward direction is caused by the reflection of downward propagating Alfv'en waves at chromospheric heights, causing an enhancement of the low-FIP elements in the corona. Since coronal waves can be produced by mechanisms that heat the solar corona, it is thought that the mechanism underlying the FIP effect is inextricably linked to processes that heat the solar corona. Hence, measuring the FIP bias is an important diagnostic for coronal plasma characteristics (Laming 2015; Dahlburg et al. 2016).

In this paper, we focus on the elemental abundances of hot, quiescent AR core emission at 3 MK, by providing line-to-continuum measurements of the Sun in the soft X-ray energy band using data from the Solar X-ray Monitor (XSM: Vadawale et al. 2014; Shanmugam et al. 2020). It may be noted here that the XSM is the only spectrometer to have observed the Sun in the 1-15 keV range during the minimum of solar cycle 24 with an energy resolution better than 180 eV at 5.9 keV. This resolution is sufficient to measure the abundances of several elements. The soft X-ray continuum is dominated by free-free radiation (with some free-bound emission, see e.g. Figure 12b of Mondal et al. 2021), which primarily originates from H. Hence, measuring the abundances of an emission line with respect to the continuum provides the absolute abundance of that element. It should be noted that the measurement of free-free emission can also be carried out in the EUV energy band, but it is limited to large flares (e.g., Feldman et al. 2003).

The XSM energy band is sensitive to temperatures above 2 MK. When the Sun was at minimum activity levels, without any ARs, the XSM observed a steady signal originating from X-ray Bright Points (XBPs), with a peak emission around 2 MK (Vadawale et al. 2021b). When a single non-flaring AR is present, the signal is dominated by the AR's near-isothermal ~ 3 MK emission (see, e.g. Del Zanna 2013). This provides an excellent opportunity to measure the FIP bias of the hot quiescent core for individual active regions during their evolution.

In the literature, very few abundance measurements are know to be associated specifically with the 3 MK emission from quiescent AR cores. These are summarised in Del Zanna and Mason (2018). X-ray spectra in the 10–20 Å range have provided the relative abundances of the low-FIP Fe, Mg vs. O, Ne. Most studies provided results on single active regions. Saba and Strong (1993) reported a significant variability of the FIP bias using SMM/FCS observations of several active regions. On the other hand, a re-analysis of several quiescent AR cores with improved atomic data and using a multi-thermal DEM technique by Del Zanna and Mason (2014) indicated the same FIP bias, around 3, for all active regions, irrespective of their age and size.

Since 2006, EUV spectra from the Hinode EIS instrument have provided an opportunity to measure the relative FIP bias between low-FIP elements (e.g. Fe, Si) and the high-FIP Ar, as well as the mid-FIP S, which actually shows the same abundance variations as the high-FIP elements. An example case was discussed by Del Zanna (2013), showing that the FIP bias in the EUV of 3 MK plasma was the same as in the X-rays. Considering the size of the emitting plasma and its emission measure, Del Zanna (2013) concluded that it should be the low-FIP elements that are over-abundant by about a factor of 3.

Del Zanna et al. (2022) carried out a multi-wavelength study of an AR as it crossed the solar disk which was observed by XSM as well as by SDO/AIA, Hinode/EIS and Hinode/XRT. The relative FIP bias obtained from Hinode/EIS observations confirmed the Del Zanna (2013) results, and showed no variation with the disk passage. The analysis of simultaneous XSM spectra on two days also indicated no significant variability, and provided an absolute FIP bias for Si of 2.4, i.e. close to the value suggested by Del Zanna (2013), and also very close to the prediction of Laming's model.

In the present study, we extend the previous XSM analysis to all the quiescent periods of the same active region, and also investigate two other active regions during their disk crossings. One AR in particular is of interest as it emerged on-disk, and hence offers the opportunity to study the elemental abundances during the early phase of the evolution of an AR.

The rest of the paper is organized as follows: Section 2 provides a short overview of previous abundance measurements in active regions. Section 3 describes the

observations and data analysis. Section 4 provides a detailed spectral analysis. After obtaining the results, these are discussed in Section 5. Section 6 provides a brief summary of the article.

2. HISTORICAL OVERVIEW

Spatially resolved measurements of the relative FIP bias have been carried out by several authors (see,e.g. Widing and Feldman 1993; Sheeley 1995, 1996; Widing 1997; Widing and Feldman 2001) using Skylab spectro-heliograms with Mg, Ne transition region lines. These are formed well below 1 MK, in the legs of active region 'cool' (1 MK) loops. They found photospheric composition (FIP bias=1) for newly emerged closed loops, but increasing FIP bias reaching a value of 3-4 within a timescale of 1-2 days (Widing and Feldman 2001), and much higher values, up to about 10, within a few more days. Differing FIP biases were also obtained by Young and Mason (1997) and Dwivedi et al. (1999) using Mg and Ne line ratios observed by the CDS and SUMER spectrometers onboard the Solar and Heliospheric Observatory (SOHO).

The large values are hard to reconcile with in-situ measurements, where the FIP bias is at most 3, and also with theory. However, Del Zanna (2003) pointed out that as the cool AR loops are almost isothermal in their cross-section, the assumption that a smooth emission measure distribution was present in the plasma, used to interpret the Skylab data, was not justified. Del Zanna (2003) took the intensities measured by Widing and Feldman (1993), and using an emission measure loci approach, showed that a FIP bias of 3.7 was consistent with the data, much lower than the value of 14 reported by Widing and Feldman. Del Zanna (2003) also analysed the legs of several cool loops observed by SoHO/CDS and found photospheric abundances, although a similar analysis for other loops by Del Zanna and Mason (2003) found a FIP bias of 4.

In summary, the legs of cool AR loops do show a range of FIP bias values, between 1 and 4, and perhaps occasionally larger. However, the very high FIP biases found from Skylab data were largely overestimated.

As shown by Del Zanna and Mason (2003), active region cores are composed not only of cool 1 MK loops and unresolved, almost isothermal 3 MK loops, but also unresolved emission in the 1–3 MK range. The plasma at different temperatures is generally not cospatial.

There is evidence from Hinode EIS observations of e.g. Si X, S X lines that this $\simeq$2 MK emission has a lower relative FIP bias, around 2 (see,e.g. Del Zanna 2012). Further studies using the same lines (e.g., Baker et al. 2013, 2015; Doschek and Warren 2019; Mihailescu et al.

2022; Ko et al. 2016; Testa et al. 2022) have shown some variation (around the value of 2) of the relative FIP bias within each active region, but little variability in time, except during the decay phase, when an AR effectively disappears and the relative abundances become photospheric.

In summary, active region structures formed at temperatures below 2 MK show a range of relative FIP biases, and some temporal variability. The few observations of the hotter, 3 MK, AR cores have in contrast shown a remarkable consistency, with relative FIP biases around 3.

Finally, to interpret observations of the Sun as a star, one needs to take into account the above (and other) issues. As shown by Del Zanna (2019), when the Sun's activity is at a minimum with no active region present on the solar disk, the corona around 1 MK shows near photospheric abundances, whereas in presence of active regions, the FIP bias for the 1 MK emission stays the same, but the hotter emission shows a higher relative FIP bias. When active regions flare, the high temperature plasma shows nearly photospheric composition around the peak X-ray emission (see e.g., Mondal et al. 2021).

3. OBSERVATIONS AND DATA ANALYSIS

Observations of the Sun were carried out with the XSM during the minimum of solar cycle 24, when no active regions were present, covering the years 2019-2020. Results are given in Vadawale et al. (2021b). They reported intermediate abundances of low-FIP elements (Mg, Al, and Si) of 2 MK plasma, primarily originating from X-ray Bright Points, XBPs (Mondal et al. 2022). Frequent micro-flaring activity was observed and found to be occurring everywhere on the solar disk, even when no ARs were present (Vadawale et al. 2021a). During the minimum of solar cycle 24, XSM observed the disk passage of a few individual, isolated ARs in the absence of any other major activity. When ARs were present on-disk, XSM recorded hundreds of small flares of different classes. Elemental abundance variations during these small flares were found, for the first time, to initially drop to photospheric values, then rapidly return to coronal values, as described by Mondal et al. (2021), Mithun et al. (2022), and Lakshitha et al. (2022). In this paper, we analyze the temporal evolution of active regions outside of flaring activity and for this we have chosen to study three isolated active regions: AR12749, AR12758, and AR12759.

XSM data contain spectra at 1 s cadence in a raw (level-1) daily file. Since the visibility of the Sun varies within the XSM field-of-view (FOV), with the Sun be-

ing sometimes outside the FOV or being occulted by the Moon, the data include both solar and non-solar spectra. The XSM Data Analysis Software (XSMDAS: Mithun et al. (2021)) has been used to generate the level-2 science data product using the appropriate Good Time Intervals (GTIs) and the other necessary instrumental parameters. The available default level-2 data contains the effective area corrected light curves for every second and spectra for every minute. XSMDAS also provides the functionality to generate the light curves and spectra for a given cadence and energy range, which we have used in the present analysis.

Using the XSMDAS, we have generated 2 min averaged XSM light curves in the energy range of 1-15 keV during the disk passage of the AR12749, AR12758, and AR12759, as shown in the three panels of Figure 1. During the evolution of these three ARs, representative full disk X-ray images taken by the XRT Be-thin filter are shown in the top row of each panel. AR12749 (Figure 1a) appeared from the east limb on Sept 29, 2019. Whilst crossing the solar disk, it became fainter towards the west limb and went behind the limb on 14 Oct. AR12758 (Figure 1b) appears to form on disk on 06 Mar 2020 and fully emerged after 08 Mar. It decays whilst crossing the solar disk and finally goes behind the west limb on 18 Mar. AR12759 appeared from the east limb on 29 Mar 2020 and transited the solar disk until 14 Apr 2020, before disappearing behind the west limb.

The full disk XRT images show that during the passage of these three ARs, no other major activity was present on the solar disk. Thus, we conclude that these three ARs were primarily responsible, during their disk passage, for the enhanced X-ray emission observed by the XSM. These ARs produced many small B/A-class flares, seen as multiple spikes in the XSM light curves. Detailed studies of these small flares were reported by Mondal et al. (2021) and Lakshitha et al. (2022).

In the present study, we have selected only the quiescent periods from the observed light curves by excluding the periods when the small flares occurred using a semi-automated graphical algorithm. For example, Figure 2 shows the representative selection (orange shaded regions) for the AR quiescent durations on 2020-04-06. These identified time intervals were used as user-defined GTIs to generate the spectra for quiescent ARs on a daily basis in order to carry out the detailed spectral analysis as discussed in Section 4.

4. SPECTRAL ANALYSIS

Broad-band soft X-ray spectra of the solar corona consist of a continuum as well as the emission lines of the different elements. Modeling the soft X-ray spectrum

provides the measurements of the temperature, emission measure, and elemental abundances (with respect to hydrogen) of the emitting plasma (Del Zanna and Mason 2018). We use the *chisoth* model (Mondal et al. 2021) for the spectral fitting. The *chisoth* is a local model of the X-ray spectral fitting package (XSPEC: Arnaud et al. (1999)), and it estimates the theoretical spectrum using the CHIANTI atomic database. It takes temperature, emission measure (EM: which is related to the density of the plasma), and the elemental abundances of the elements from Z=2 to Z=30 as free variables for the spectral fitting.

After generating the spectra for the quiescent periods, we fitted them with an isothermal emission model. For the spectral fitting, we ignored the spectra below 1.3 keV where the XSM response is not well-known (Mithun et al. 2020), and above the energy where the solar spectrum is dominated by the non-solar background spectrum. During the spectral fitting, the temperature, EM, along with the abundances of Mg, Al, and Si (whose emission lines are prominent in the XSM spectrum) were kept as variable parameters. The 1σ uncertainty of each free parameter was also estimated using the standard procedure in XSPEC.

Although the S line complex is visible in the spectra, including it in the spectral fits as a free parameter causes a large uncertainty in the measurement of the S abundance because of its poor statistics. Hence, we fixed the S abundances along with the abundances of other elements (whose emission lines are not visible in the observed spectra) with the coronal abundances of Feldman (1992). However, we found that the measurement of the S abundance is possible for the summed spectrum of the entire AR period.

Figure 3 shows the representative XSM spectra, for the three ARs fitted, in different colours, with an isothermal model. The points with error bars represent the observed spectra, whereas the solid curves represent the best-fit modeled spectra. The grey error bars represent the non-solar background spectrum, which is subtracted from the observed spectra during the spectral analysis. The lower panel shows the residual between the observed and model spectra. We have fitted all the spectra in a similar way and found that all of them are well described by isothermal model.

The X-rays observed by XSM originated from both the AR and the background quiet Sun regions (outside the AR). To determine how much emission is due to the background quiet Sun regions, we estimate the average quiet Sun spectrum using an average quiet-Sun temperature, EM, and abundances, as reported by Vadawale et al. (2021b). The average quiet Sun spectrum is shown
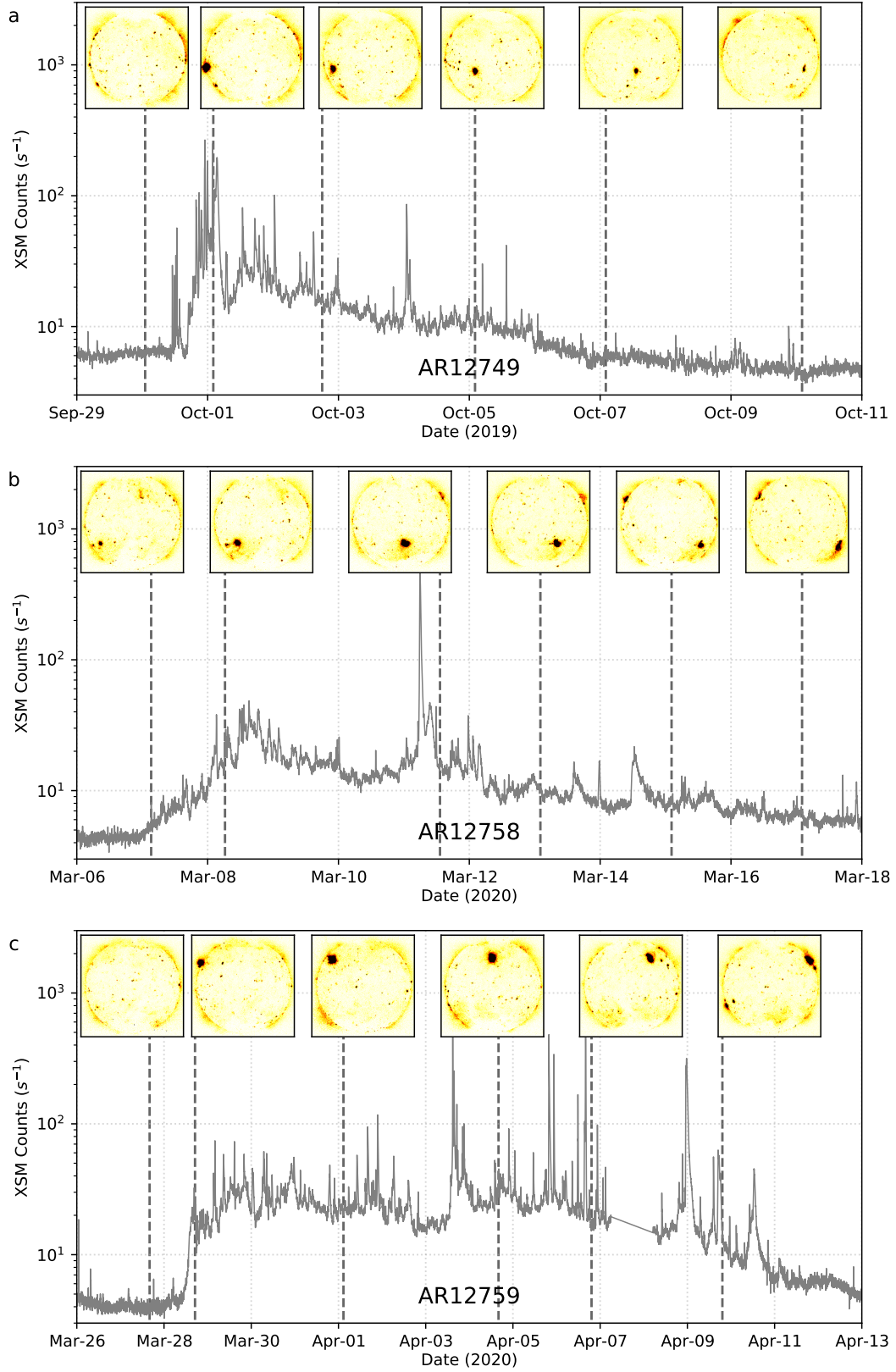
Figure 1. XSM 1-15 keV light curves during the disk passage of AR12749 (panel a), AR12758 (panel b) and AR12759 (panel c). The top row of each panel shows representative full disk X-ray images (negative intensities) taken with the XRT Be-thin filter during the evolution of the ARs. The vertical dashed lines represent the timing of the XRT images.
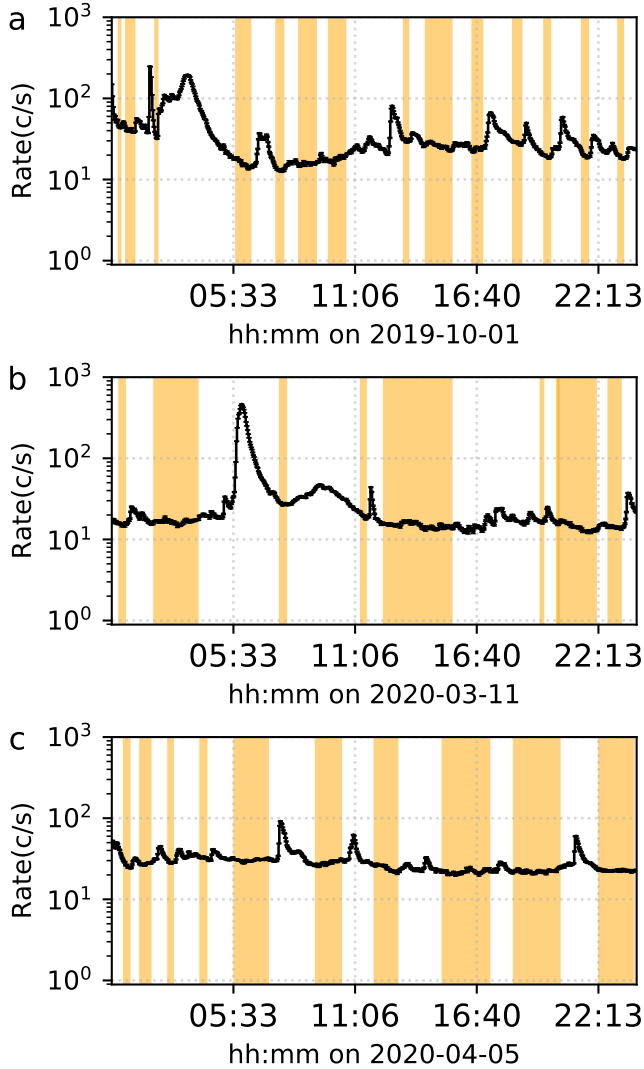
Figure 2. Selection of the quiescent AR periods (orange-shaded regions) from the XSM light-curves for one representative day of AR12749 (panel a), AR12758 (panel b), and AR12759 (panel c).

by the black dashed curve in Figure 3. The quiet Sun spectrum is found to be almost an order of magnitude lower than the spectra of the active period when the ARs were very bright on the solar disk. We thus conclude that the X-ray emission of the active periods is primarily dominated by the AR emission.

Separating the AR emission from the background quiet Sun emission would be possible by subtracting the quiet-sun spectra from the AR spectra. But, as the effective area of the XSM varies with time, this is not recommended. It is possible to model the AR spectra using a two-temperature (2T) component model rather

than subtracting the quiet Sun spectra. This is what we have chosen to do. One temperature corresponds to the background solar emission originating from the regions outside the AR and the second temperature corresponds to the AR plasma. We have modeled a few AR spectra with a two-temperature (2T) model. During the 2T spectral fitting, the parameters of the background solar emission were kept fixed to the average quiet-Sun values reported by Vadawale et al. (2021b). For the AR component, the temperature, EM, along with the abundances of Mg, Al, and Si, were kept as variable parameters. We found that the 2T model can describe the XSM spectra for the active periods with similar best-fitted parameters as those obtained by the isothermal model. This verifies that the AR emission dominates the spectra of the AR periods. Thus, in this study, we show the results of the isothermal analysis in Figure 5 and 6. This is discussed in Section 5.

It is interesting to study how the plasma parameters vary during the emerging phase of the AR12758, i.e., from 07-Mar-2020 to 09-Mar-2020. Figure 4 shows the evolution of the photospheric magnetograms (top row) and the X-ray emission (bottom row) as observed by SDO/HMI and the Be-thin filter of Hinode/XRT respectively. These images were created by de-rotating the synoptic data of HMI[1] and XRT[2] to a common date (08-Mar-2020) using the standard procedure of Solar-SoftWare (SSW; Freeland and Handy 1998). We also determined the total unsigned photospheric magnetic flux for the regions ± 10 G within the field-of-view shown in Figure 4. During this emerging flux period, we carried out a time-resolved spectroscopic study using the XSM observations with finer time bins of less than a day. However, during this period, as the emission from the AR was not very bright, the emission from the AR and the rest of the Sun could be mixed together. Thus to derive the evolution of the plasma parameters during this period, we modeled the observed XSM spectra with a 2T model, where one component represents the emission from the AR, and the other represents the emission from the rest of the Sun, as discussed in the previous paragraph. The results are shown in Figure 7 and discussed in Section 5.

5. RESULTS AND DISCUSSION

In this study, we have performed the X-ray spectral analysis for the evolution of three ARs as observed by the XSM. The AR spectra (Figure 3) show a clear signature of the thermal X-ray emission from the line com-

[1] http://jsoc.stanford.edu/data/hmi/synoptic/

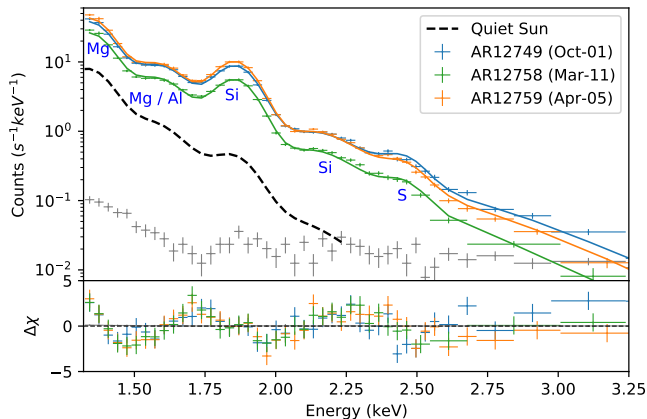[2] http://solar.physics.montana.edu/HINODE/XRT/SCIA/

Figure 3. Soft X-ray spectra measured by the XSM for three representative days of the AR period are shown. Solid lines represent the best-fit isothermal model, and the residuals are shown in the bottom panel. Gray points correspond to the non-solar background spectrum.

plexes of Mg, Al, Si, and S, along with the continuum emission up to ∼3.0 keV. The red points in Figure 5 show the evolution of the temperature and EM throughout the evolution of the three ARs. Figure 6 shows the evolution of abundances of Mg (panel a), Al (panel b), and Si (panel c). The error bars associated with all the parameters along the y-axis represent the 1σ uncertainties. We also derived the average S abundance along with the other elements from the summed spectrum for the duration when the ARs were very bright on the solar disk (bounded by the vertical dashed lines in Figures 5 and 6). This provides the average parameters associated with each AR, as shown by magenta bars and also given in Table 1. The primary findings of the paper are discussed below.

5.1. *Temperature and emission measure*

Temperatures (T) and emission measures (EM) are close to the quiet Sun levels (black dashed lines in Figure 5) when the ARs were absent from the solar disc or only partially present, e.g., 30 September 2019 and 6 March 2020. Once the ARs appear, the temperature rises to more than ∼3 MK from the ∼2 MK of the quiet Sun. As the ∼3 MK emission is predominantly derived from a smaller volume of AR plasma, the presence of the AR reduces the EM from the quiet Sun values. The average temperatures for all the ARs are determined to be ∼3 MK (blue error bars in Figure 5a), which is close to the "basal" temperature of the AR core reported in earlier research (e.g., Del Zanna and Mason 2018; Del Zanna 2012; Winebarger et al. 2012). The temperature and EM do, however, vary slightly over the course of the

AR's evolution, which is consistent with the observed X-ray light curve. Following the arrival of AR12749 and AR12758, their activity decayed while rotating on the solar disk (Figure 1), which is why the temperature and EM decreased during their evolution, as indicated by the dashed vertical lines in Figure 5. After October 6, 2019, the EM for AR12749 begins to rise as the AR weakens and the quiet Sun emission takes precedence over the AR emission. Thus, after the AR has almost died and is very faint, the EM and temperature reach values close to the quiet Sun temperature and EM. The temperature and EM for the AR12759 remain almost constant with time, as this AR crossed the solar disk without much decay in activity (Figure 1c).

5.2. *Abundance evolution*

In contrast to the temperature and EM, the abundances of Mg, Al, and Si do not follow the X-ray light curve of any of the three ARs throughout their evolution (Figure 6). The abundances obtained for low-FIP elements Al, Mg, and Si are consistently greater than the photospheric values, demonstrating a persistent FIP bias during the course of the AR. After the emergence of AR12758, the FIP bias is found to be almost constant throughout its decay phase. Similarly, during the decay of the AR12749, the FIP bias remains nearly constant, in contrast to certain earlier studies, such as Ko et al. (2016). They suggested decreasing FIP bias in high-temperature plasma of more than two million degrees during the decay phase of an AR. The more established AR, AR12759, which evolved without decaying much during its transit across the solar disk, also shows an almost constant FIP bias, similar to the other two ARs.

We do not find any relationship between the age of the AR and the FIP bias, as suggested in some previous papers, e.g.,Del Zanna and Mason 2014; Doschek and Warren 2019. The measured abundances for Mg, Si, and S are comparable to those given by (Feldman 1992) and Fludra and Schmelz (1999) (orange shaded regions in Figure 6). However, the Al abundance is ∼30%-60% higher than the coronal abundances reported in the literature. We note that the Al lines in the XSM spectra are blended with Mg lines. From Markov Chain Monte Carlo (MCMC) analysis (discussed in Appendix A), we find that there is no anti-correlation between Mg and Al abundances. This suggests that the observed spectra does indeed require higher abundances of Al and cannot be explained by an enhancement of Mg abundances.

5.3. *FIP bias at the onset of AR core*

Though we do not find any relationship between the age of the AR cores and their FIP biases (Section 5.2),
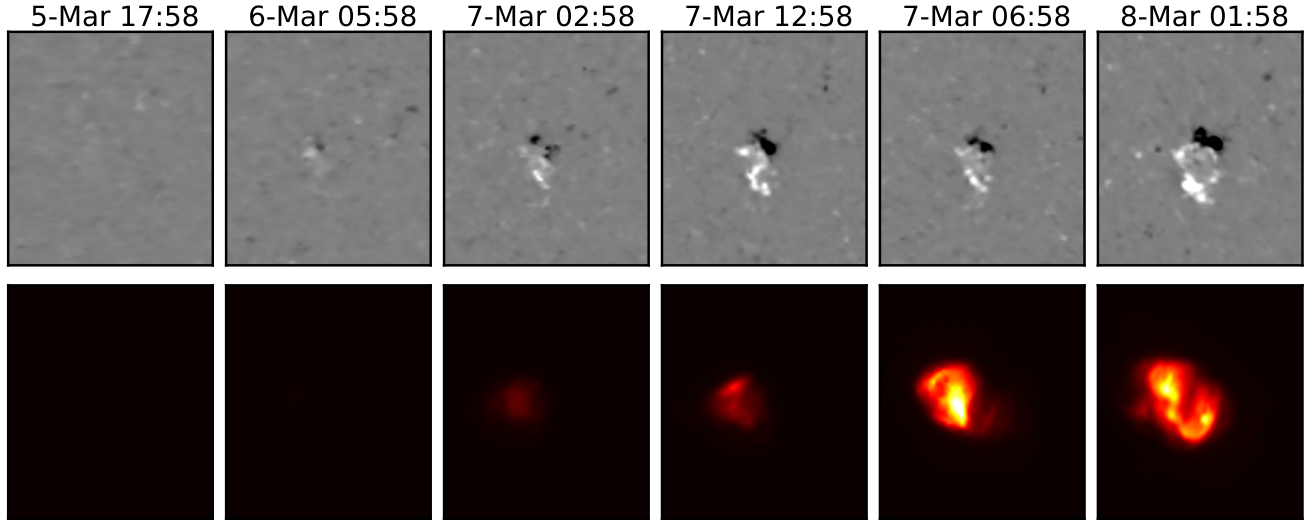
Figure 4. Evolution of the AR12758 during its emergence phase on the solar disk. Top row shows the evolution of photospheric magnetograms as observed by HMI and bottom row shows the evolution of X-ray emission as observed by XRT Be-thin filter.
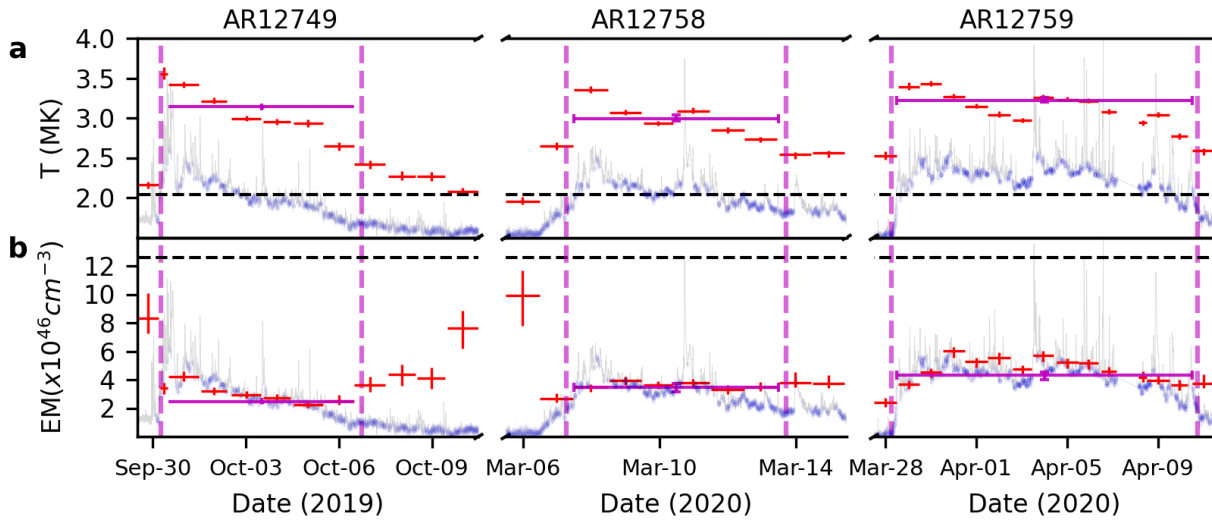

Figure 5. Evolution of the temperature (red points in panel a) and EM (red points in panel b) during the evolution of AR12749, AR12758, and AR12759. When the ARs were very bright, as bounded by the vertical dashed lines, the magenta bars represent the average values of the temperature and EM. The black horizontal dashed lines represent the average temperature and emission measure for the quiet Sun in the absence of any AR reported by Vadawale et al. (2021b). The XSM lightcurves of the ARs are shown in grey color, and the lightcurves for the quiescent regions are shown in blue colors.

which remain constant, it is interesting to study the timescale on which the FIP bias developed during the emergence of the AR core. Such a study has been made possible using the finer (< one day) time-resolved spectroscopy during the emerging phase (07-Mar-2020 to 09-Mar-2020) of AR12758. During this period, we estimated the total unsigned photospheric magnetic flux as measured by HMI/SDO and shown in Figure 7a (black

color). The peak in the magnetic flux represents the time when the AR completely emerged into the solar disk.

After the emergence, the unsigned magnetic flux is found to (temporarily) decrease. Figures 7b and 7c show the evolution of the AR core temperature and emission-measure. With the emergence of the AR. The temperature becomes close to the AR core temperature of ∼3
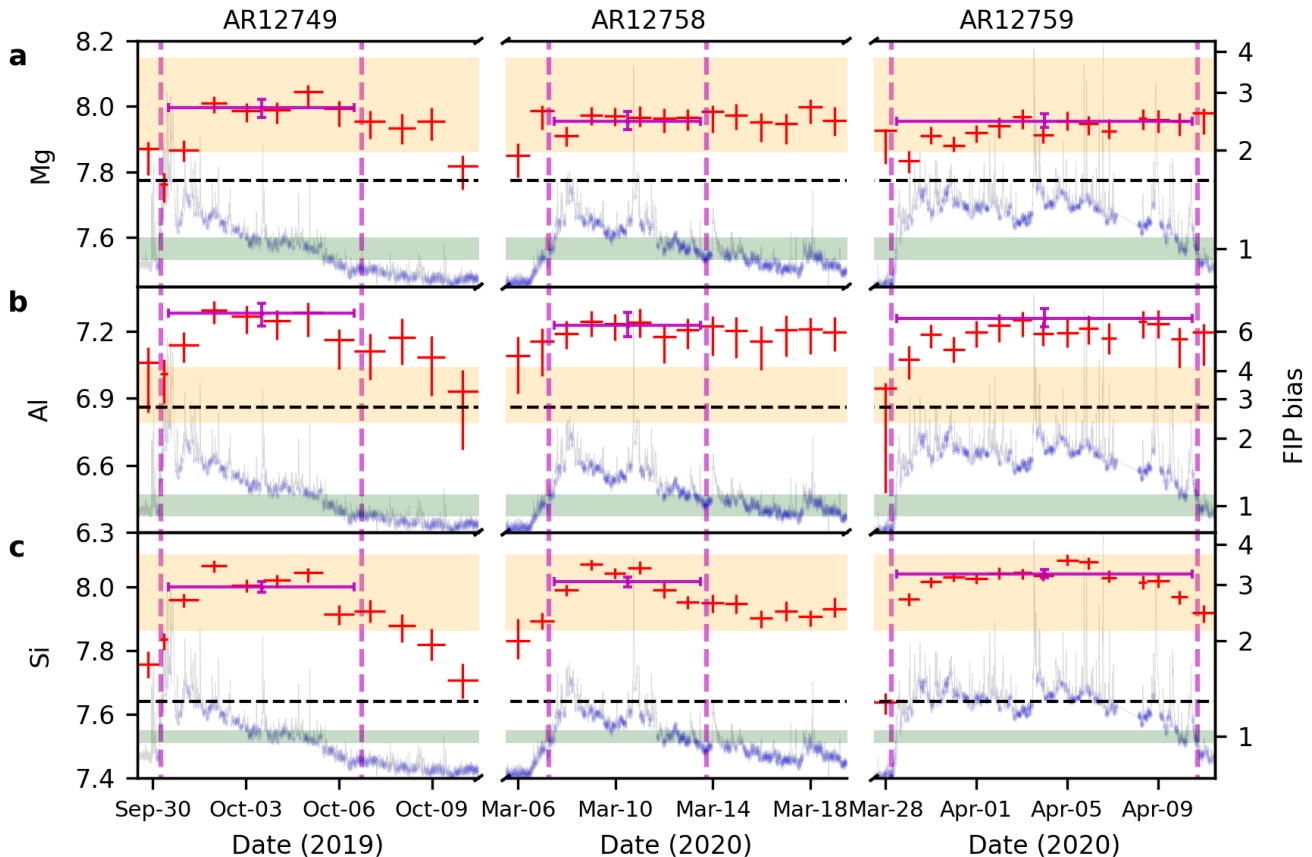
Figure 6. Panels a-c (red error bars) show the evolution of abundance in the logarithmic scale with A(H)=12 for Mg, Al, and Si during the evolution of AR12749, AR12758 and AR12759. The magenta bars represented the average abundances when the ARs were very bright, as bounded by the vertical dashed lines. The y-error bars represent 1σ uncertainty for each parameter, and the x-error bars represent the duration over which a given spectrum is integrated. The black horizontal dashed lines represent the average abundances for the quiet Sun in the absence of any AR reported by Vadawale et al. (2021b). XSM light curves for each AR are shown in gray in the background, and the blue color on the XSM light curves represents the time duration excluding the flaring activities. The range of coronal and photospheric abundances from various authors compiled in the CHIANTI database are shown as orange and green bands. The right y-axis shows the FIP bias values for the respective elements with respect to average photospheric abundances.

MK, and the EM increases as the emitting plasma volume increase until it has emerged completely. We also derived the evolution of the FIP bias during this period, shown in Figure 7d for Si. During this period, as the emission from the Mg and Al line complex was weak compared with the background solar emission, the derived FIP bias for Mg and Al has a large uncertainty and is not shown here. Within ∼10 hours of the AR emergence, the FIP bias was already close to 3, and remained almost constant throughout the evolution. So the emerging hot core loops do not show any variation, in agreement with previous suggestions. Recall that the variations in FIP bias reported earlier (e.g., Widing and Feldman 2001) were observed in the cool loops, not the core loops.

5.4. *Enhanced bias for Al*

Figure 8 shows the average values of the FIP bias (relative to the photospheric abundance Asplund et al. (2009)) for all the elements as a function of their FIP values. The lower FIP element, Al (FIP = 5.99), is found to have the highest FIP bias of 6-7, whereas the low-FIP elements, Mg (FIP = 7.65) and Si (FIP = 8.15), are found to have a lower FIP bias of ∼3. The mid/high FIP element, S, is found to have a much lower FIP bias of a factor of ∼ 1.5. A higher FIP bias for Al is noteworthy and may point to an intriguing physical process. However, this may also be a modeling artifact.

One of the possibilities could be due to missing flux caused by the presence of multi-thermal plasma providing strong signals from emission lines of Al or Mg formed
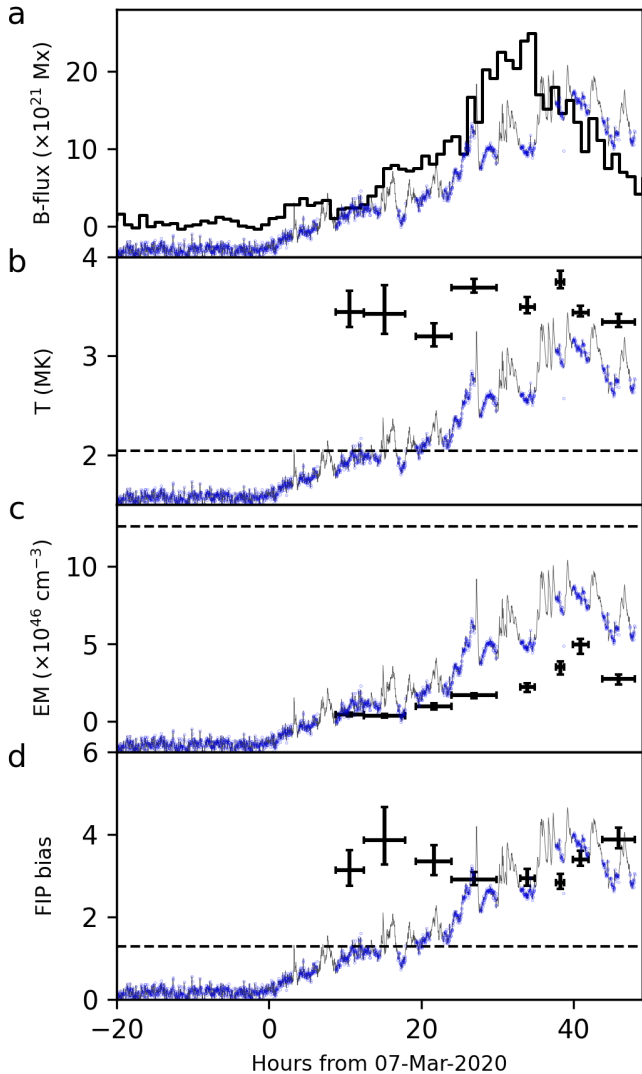
Figure 7. Results showing the emerging phase of AR12758. The black curve in panel a shows the evolution of the total unsigned photospheric magnetic flux. Panel b and c show the evolution of temperature and EM. Panel d shows the evolution of FIP bias for Si. The dashed lines in panels b-d represent the corresponding parameter for the background solar emission from the rest of the solar-disk except AR. The background grey curves in each panel represent the X-ray light curve observed by XSM. Whereas the blue curves represent the selected times excluding the flaring period, representing the quiescent AR.

at different temperatures. To verify this we have simulated the emission lines in the energy range of the Mg/Al line complex by considering the isothermal model and a multi-thermal model using the AR DEM of AR12759, reported by Del Zanna et al. (2022) (see Figure B.1 in Appendix B). Similar line intensities from various ion-

ization stages of Al and Mg can be seen in both the isothermal and multi-thermal models, confirming that the absence of the flux is not the result of multi-thermal plasma.

Another possibility is that missing flux is caused by missing lines of Al or Mg (mostly satellite lines) that are not yet present in CHIANTI version 10. We have analysed the high-resolution spectroscopic observations described by Walker et al. (1974) and found several observed lines that are missing in the database. However, the total missing flux, compared to the predicted flux by CHIANTI is not enough to explain the anomalous Al abundance. However, the Walker et al. (1974) observations were taken during a high level of solar activity, so it is possible that the missing lines have a stronger contribution at 3 MK. The Al abundance is currently clearly overestimated by some degree.

Although this analysis is not conclusive enough to rule out Al's high FIP bias as an artifact, it is also not sufficient to conclude that it is not real. A higher Al FIP bias could be real. This might be explained by examining a few particular scenarios from the Ponderomotive force model (Laming 2015) proposed by Laming (private communication), which could be investigated in a subsequent study.

We have also compared the AR core FIP bias obtained with that of the different solar activity levels measured by the XSM in previous research. These are overplotted in Figure 8. The blue points show the FIP bias during the quiet Sun period, which is dominated by X-ray Bright Points (XBP), as reported by Vadawale et al. (2021b). While the green points depict the FIP bias during the peak of the solar flares as reported by Mondal et al. (2021). The FIP bias of the AR core (red points) shows a consistently higher value for the elements Al, Mg, and Si compared with the FIP bias of XBPs (green points). Since ARs have substantially higher magnetic activity than the XBPs, the increased FIP bias of the ARs relative to the XBPs is expected from the Ponderomotive force model. On the other hand, chromospheric evaporation during the flaring mechanism results in a near unit FIP bias during the peak of the flares (Mondal et al. 2021).

6. SUMMARY

We present the evolution of plasma characteristics for three ARs using disk-integrated soft X-ray spectroscopic observations from the XSM to make simultaneous line and continuum measurements. Carrying out a comprehensive study of an AR using the Sun-as-a-star mode observation is challenging because of the presence of multiple activities throughout the solar cycle. Unique

Table 1. Best fitted parameters for the average spectrum of each AR.

AR	T (MK)	EM (10^{46} cm^{-3})	Mg	Al	Si	S
12749	$3.14^{+0.04}_{-0.05}$	$2.46^{+0.24}_{-0.19}$	$8.00^{+0.02}_{-0.03}$	$7.28^{+0.05}_{-0.06}$	$8.00^{+0.02}_{-0.02}$	$7.23^{+0.06}_{-0.05}$
12759	$3.22^{+0.04}_{-0.02}$	$4.30^{+0.21}_{-0.28}$	$7.95^{+0.02}_{-0.02}$	$7.26^{+0.04}_{-0.04}$	$8.04^{+0.01}_{-0.01}$	$7.23^{+0.02}_{-0.03}$
12758	$2.99^{+0.05}_{-0.03}$	$3.48^{+0.25}_{-0.31}$	$7.95^{+0.03}_{-0.02}$	$7.23^{+0.06}_{-0.05}$	$8.02^{+0.02}_{-0.02}$	$7.32^{+0.05}_{-0.06}$
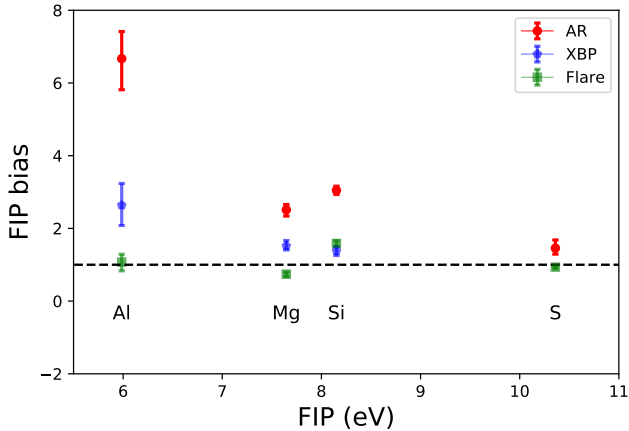
Figure 8. Variation of the FIP bias with the FIP of the elements. The red points are the averaged FIP bias for the ARs reported in the present study. The blue points are the FIP bias for the XBPs as reported by Vadawale et al. (2021b). The green points are the measured FIP bias during the peak of solar flares as reported by Mondal et al. (2021).

XSM observations made during the minimum of Solar Cycle 24 allowed the study of the evolution of temperature, EM, and the abundances of Mg, Al, and Si for the individual ARs in the absence of any other noteworthy activity on the solar disk. Since the ARs were the principal contributors of disk-integrated X-rays during their evolution, the temperature and EM followed their X-ray light curve. The average temperature of all the AR is ~3 MK, close to the well-known temperature of the AR core. Irrespective of the activity and age of the ARs, the abundances or the FIP biases of Al, Mg, and Si were found to be consistently greater than their photospheric values without much variation. The abundance values develop within ~10 hours of the appearance of the AR during its emerging phase. Throughout the AR evolution, the low FIP elements, Mg and Si, have a FIP bias close to 3, whereas the mid-FIP element, S, has an average FIP bias of ~1.5. The lowest FIP element, Al, has a greater FIP bias of ~6-7. After discussing vari-

ous modeling artifacts, the Al abundance appears to be overestimated, although the exact factor is unknown. Increased Al abundance could be real, implying that low-FIP elements degree of FIP bias is linked to their FIP values. Future spectroscopic studies to measure the FIP bias for more low-FIP elements (for example, Ca, whose FIP bias is between Al and Mg) would help us to better understand this phenomenon. In this regard, recent and upcoming X-ray spectrometers (for example, DAXSS: (Schwab et al. 2020) onboard INSPIRESat-1, SoLEXS (Sankarasubramanian et al. 2011) onboard upcoming Aditya-L1 observatory, and rocket-borne spectrometer MaGIXS (Champey et al. 2022)) will be useful.

APPENDIX

A. RESULTS OF MCMC ANALYSIS

We carried out Markov Chain Monte Carlo (MCMC) analysis of the spectra to obtain the regions of parameter space that best fits the observed spectra. This was done using the 'chain' method available within XSPEC. Figure A1 shows the corner plot of the results for the spectrum on 01-Oct-2019. The results show that all parameters are well constrained by the spectra. Particularly, we note that there is no anti-correlation observed between Al and Mg abundances showing that the enhances Al abundances obtained cannot be adjusted by enhancements in Mg abundances. Similar trends are observed for spectra of other days as well.
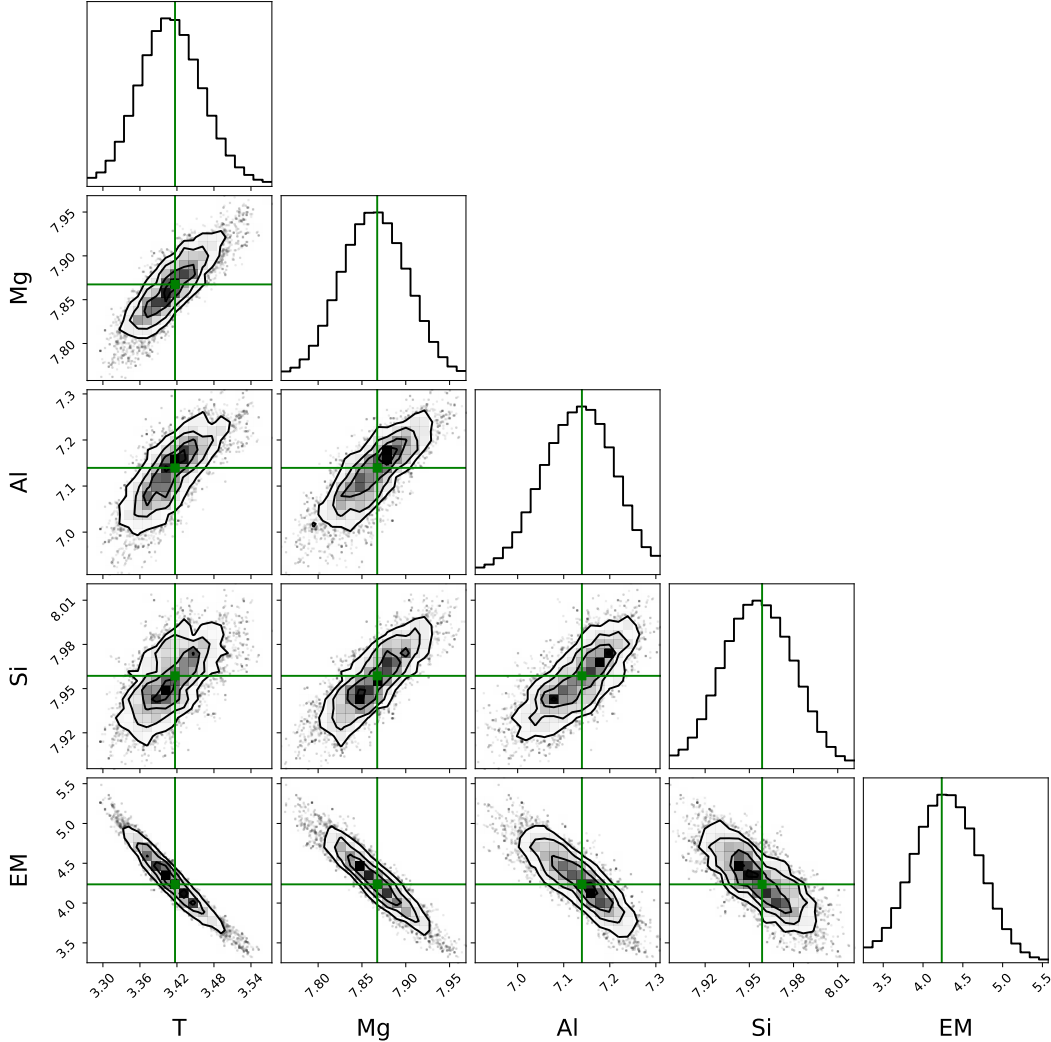

Figure A.1. Corner plot depicting the results of MCMC analysis for the fitted spectrum on 01-Oct-2019. The histograms depict the marginalized distribution associated with each parameter. The scatter-plots are overlaid with contours representing 1σ, 2σ, and 3σ levels to show correlations between all parameters. The best-fit parameters are represented by green lines.

B. SIMULATED SPECTRUM

To check the effect of temperatures on the Mg/Al line fluxes in the XSM energy range of 1.55 to 1.70 keV, we have compared the simulated spectra in the same energy range by considering the isothermal and multi-thermal DEM models. Figure B.1 shows the simulated 3 MK spectrum (blue) overplotted with the multithermal spectrum (red). The isothermal spectrum is generated for an emission measure of 10^{27} cm^{-5}. The multithermal spectrum is derived by
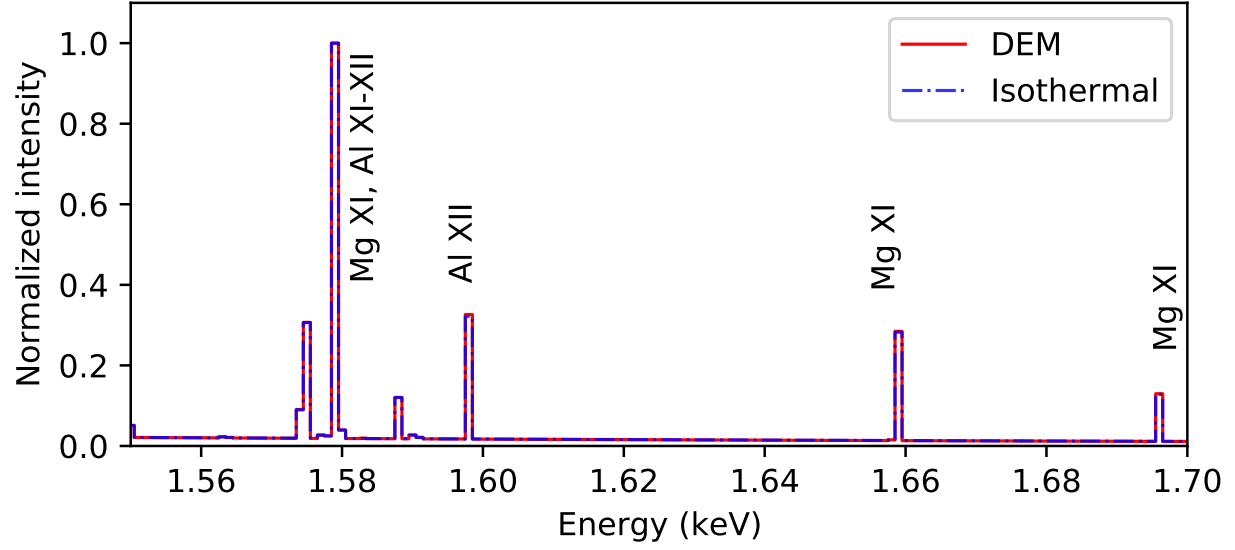
Figure B.1. Simulated spectra from CHIANTI v 10 in the energy range of Mg/Al line complex of XSM observed spectrum. Solid blue curve show the multi-thermal spectrum and dashed orange curve shows the isothermal spectrum.

using the reported quiescent AR DEM by Del Zanna et al. (2022), which was obtained from the Hinode EIS observation of AR12759. For the comparison of both spectra, we have normalized them with the corresponding line flux of Mg XI, and Al XI-XII. Similar line intensities predicted by both isothermal and multithermal models indicates that spectra are insensitive to temperature in this case.

REFERENCES

Arnaud, K., Dorman, B., and Gordon, C. (1999). XSPEC: An X-ray spectral fitting package.

Asplund, M., Grevesse, N., Sauval, A. J., and Scott, P. (2009). The Chemical Composition of the Sun. *ARA&A*, 47(1):481–522.

Baker, D., Brooks, D. H., Démoulin, P., van Driel-Gesztelyi, L., Green, L. M., Steed, K., and Carlyle, J. (2013). Plasma Composition in a Sigmoidal Anemone Active Region. *ApJ*, 778(1):69.

Baker, D., Brooks, D. H., Démoulin, P., Yardley, S. L., van Driel-Gesztelyi, L., Long, D. M., and Green, L. M. (2015). FIP Bias Evolution in a Decaying Active Region. *ApJ*, 802(2):104.

Baker, D., Brooks, D. H., van Driel-Gesztelyi, L., James, A. W., Démoulin, P., Long, D. M., Warren, H. P., and Williams, D. R. (2018). Coronal Elemental Abundances in Solar Emerging Flux Regions. *ApJ*, 856(1):71.

Bochsler, P. (2007). Minor ions in the solar wind. *A&A Rv*, 14(1):1–40.

Brooks, D. H., Baker, D., van Driel-Gesztelyi, L., and Warren, H. P. (2017). A solar cycle correlation of coronal element abundances in sun-as-a-star observations. *Nature Communications*, 8(1).

Brooks, D. H., Ugarte-Urra, I., and Warren, H. P. (2015). Full-Sun observations for identifying the source of the slow solar wind. *Nature Communications*, 6:5947.

Brooks, D. H. and Warren, H. P. (2011). Establishing a Connection Between Active Region Outflows and the Solar Wind: Abundance Measurements with EIS/Hinode. *ApJL*, 727(1):L13.

Champey, P. R., Winebarger, A. R., Kobayashi, K., Athiray, P. S., Hertz, E., Savage, S., Beabout, B., Beabout, D., Broadway, D., Bruccoleri, A. R., Cheimets, P., Davis, J., Duffy, J., Golub, L., Gregory, D. A., Griffith, C., Haight, H., Heilmann, R. K., Hogue, B., Hohl, J., Hyde, D., Kegley, J., Kolodzieczjak, J., Ramsey, B., Ranganathan, J., Robertson, B., Schattenburg, M. L., Speegle, C. O., Vigil, G., Walsh, R., Weddenorf, B., and Wright, E. (2022). The Marshall Grazing Incidence X-ray Spectrometer (MaGIXS). *Journal of Astronomical Instrumentation*, 11(2):2250010.

Dahlburg, R. B., Laming, J. M., Taylor, B. D., and Obenschain, K. (2016). PONDEROMOTIVE ACCELERATION IN CORONAL LOOPS. *The Astrophysical Journal*, 831(2):160.

Del Zanna, G. (2003). Solar active regions: The footpoints of 1 MK loops. *A&A*, 406:L5–L8.

Del Zanna, G. (2012). Benchmarking atomic data for the CHIANTI atomic database: coronal lines observed by Hinode EIS. *A&A*, 537:A38.

Del Zanna, G. (2013). The multi-thermal emission in solar active regions. *A&A*, 558:A73.

Del Zanna, G. (2019). The EUV spectrum of the Sun: Quiet- and active-Sun irradiances and chemical composition. *A&A*, 624:A36.

Del Zanna, G. and Mason, H. E. (2003). Solar active regions: SOHO/CDS and TRACE observations of quiescent coronal loops. *A&A*, 406:1089–1103.

Del Zanna, G. and Mason, H. E. (2014). Elemental abundances and temperatures of quiescent solar active region cores from X-ray observations. *A&A*, 565:A14.

Del Zanna, G. and Mason, H. E. (2018). Solar UV and X-ray spectral diagnostics. *Living Reviews in Solar Physics*, 15(1):5.

Del Zanna, G., Mondal, B., Rao, Y. K., Mithun, N. P. S., Vadawale, S. V., Reeves, K. K., Mason, H. E., Sarkar, A., Janardhan, P., and Bhardwaj, A. (2022). Multiwavelength Observations by XSM, Hinode, and SDO of an Active Region. Chemical Abundances and Temperatures. *ApJ*, 934(2):159.

Doschek, G. A. and Warren, H. P. (2019). The Variability of Solar Coronal Abundances in Active Regions and the Quiet Sun. *ApJ*, 884(2):158.

Dwivedi, B. N., Curdt, W., and Wilhelm, K. (1999). Analysis of Extreme-Ultraviolet Off-Limb Spectra Obtained with SUMER/SOHO: Ne VI-Mg VI Emission Lines. *ApJ*, 517(1):516–525.

Feldman, U. (1992). Elemental abundances in the upper solar atmosphere. *PhyS*, 46(3):202–220.

Feldman, U., Landi, E., Doschek, G. A., Dammasch, I., and Curdt, W. (2003). Free-Free Emission in the Far-Ultraviolet Spectral Range: A Resource for Diagnosing Solar and Stellar Flare Plasmas. *ApJ*, 593(2):1226–1241.

Feldman, U., Schuhle, U., Widing, K. G., and Laming, J. M. (1998). Coronal composition above the solar equator and the north pole as determined from spectra acquired by the SUMER instrument onSOHO. *The Astrophysical Journal*, 505(2):999–1006.

Feldman, U. and Widing, K. G. (2002). A review of the first ionization potential effect on elemental abundances in the solar corona and in flares. *Physics of Plasmas*, 9(2):629–635.

Fludra, A. and Schmelz, J. T. (1999). The absolute coronal abundances of sulfur, calcium, and iron from Yohkoh-BCS flare spectra. *A&A*, 348:286–294.

Freeland, S. L. and Handy, B. N. (1998). Data Analysis with the SolarSoft System. *SoPh*, 182(2):497–500.

Gloeckler, G. and Geiss, J. (1989). The abundances of elements and isotopes in the solar wind. In Waddington, C. J., editor, *Cosmic Abundances of Matter*, volume 183 of *American Institute of Physics Conference Series*, pages 49–71.

Ko, Y.-K., Young, P. R., Muglach, K., Warren, H. P., and Ugarte-Urra, I. (2016). Correlation of Coronal Plasma Properties and Solar Magnetic Field in a Decaying Active Region. *ApJ*, 826(2):126.

Lakshitha, N., Mondal, B., Narendranath, S., and Paul, K. (2022). Elemental abundances during A-class solar flares: Soft X-ray spectroscopy from Chandrayaan-2 XSM. *Under preparation.*

Laming, J. M. (2004). A Unified Picture of the First Ionization Potential and Inverse First Ionization Potential Effects. *ApJ*, 614(2):1063–1072.

Laming, J. M. (2009). Non-Wkb Models of the First Ionization Potential Effect: Implications for Solar Coronal Heating and the Coronal Helium and Neon Abundances. *ApJ*, 695(2):954–969.

Laming, J. M. (2012). Non-WKB Models of the First Ionization Potential Effect: The Role of Slow Mode Waves. *ApJ*, 744(2):115.

Laming, J. M. (2015). The fip and inverse fip effects in solar and stellar coronae. *Living Reviews in Solar Physics*, 12:1–76.

Laming, J. M. (2017). The first ionization potential effect from the ponderomotive force: On the polarization and coronal origin of alfvén waves. *The Astrophysical Journal*, 844(2):153.

Mihailescu, T., Baker, D., Green, L. M., van Driel-Gesztelyi, L., Long, D. M., Brooks, D. H., and To, A. S. H. (2022). What Determines Active Region Coronal Plasma Composition? *ApJ*, 933(2):245.

Mithun, N., Vadawale, S., Patel, A., Shanmugam, M., Chakrabarty, D., Konar, P., Sarvaiya, T., Padia, G., Sarkar, A., Kumar, P., Jangid, P., Sarda, A., Shah, M., and Bhardwaj, A. (2021). Data processing software for chandrayaan-2 solar x-ray monitor. *Astronomy and Computing*, 34:100449.

Mithun, N. P. S., Vadawale, S. V., Sarkar, A., Shanmugam, M., Patel, A. R., Mondal, B., Joshi, B., Janardhan, P., Adalja, H. L., Goyal, S. K., Ladiya, T., Tiwari, N. K., Singh, N., Kumar, S., Tiwari, M. K., Modi, M. H., and Bhardwaj, A. (2020). Solar X-Ray Monitor on Board the Chandrayaan-2 Orbiter: In-Flight Performance and Science Prospects. *SoPh*, 295(10):139.

Mithun, N. P. S., Vadawale, S. V., Zanna, G. D., Rao, Y. K., Joshi, B., Sarkar, A., Mondal, B., Janardhan, P., Bhardwaj, A., and Mason, H. E. (2022). Soft X-Ray Spectral Diagnostics of Multithermal Plasma in Solar Flares with Chandrayaan-2 XSM. *ApJ*, 939(2):112.

Mondal, B., Klimchuk, J. A., Vadawale, S. V., Sarkar, A., Zanna, G. D., Athiray, P. S., Mithun, N., Mason, H. E., and Bhardwaj, A. (2022). Role of small-scale impulsive events in heating the X-ray bright points of the quiet Sun. *Submitted to ApJ.*

Mondal, B., Sarkar, A., Vadawale, S. V., Mithun, N. P. S., Janardhan, P., Del Zanna, G., Mason, H. E., Mitra-Kraev, U., and Narendranath, S. (2021). Evolution of Elemental Abundances during B-Class Solar Flares: Soft X-Ray Spectral Measurements with Chandrayaan-2 XSM. *ApJ*, 920(1):4.

Pottasch, S. R. (1963). The Lower Solar Corona: Interpretation of the Ultraviolet Spectrum. *ApJ*, 137:945.

Saba, J. L. R. and Strong, K. T. (1993). Coronal abundances of O, Ne, Mg, and Fe in solar active regions. *Advances in Space Research*, 13(9):391–394.

Sankarasubramanian, K., Ramadevi, M. C., Bug, M., Umapathy, C. N., Seetha, S., Sreekumar, P., and Kumar (2011). SoLEXS - A low energy X-ray spectrometer for solar coronal studies. In *Astronomical Society of India Conference Series*, volume 2 of *Astronomical Society of India Conference Series*, pages 63–69.

Schwab, B. D., Sewell, R. H. A., Woods, T. N., Caspi, A., Mason, J. P., and Moore, C. (2020). Soft X-Ray Observations of Quiescent Solar Active Regions Using the Novel Dual-zone Aperture X-Ray Solar Spectrometer. *ApJ*, 904(1):20.

Shanmugam, M., Vadawale, S. V., Patel, A. R., Adalaja, H. K., Mithun, N. P. S., Ladiya, T., Goyal, S. K., Tiwari, N. K., Singh, N., Kumar, S., Painkra, D. K., Acharya, Y. B., Bhardwaj, A., Hait, A. K., Patinge, A., Kapoor, A. h., Kumar, H. N. S., Satya, N., Saxena, G., and Arvind, K. (2020). Solar X-ray Monitor Onboard Chandrayaan-2 Orbiter. *Current Science*, 118(1):45–52.

Sheeley, N. R., J. (1995). A Volcanic Origin for High-FIP Material in the Solar Atmosphere. *ApJ*, 440:884.

Sheeley, N. R., J. (1996). Elemental Abundance Variations in the Solar Atmosphere. *ApJ*, 469:423.

Testa, P., Martinez-Sykora, J., and De Pontieu, B. (2022). Coronal Abundances in an Active Region: Evolution and Underlying Chromospheric and Transition Region Properties. *arXiv e-prints*, page arXiv:2211.07755.

Vadawale, S., Shanmugam, M., Acharya, Y., Patel, A., Goyal, S., Shah, B., Hait, A., Patinge, A., and Subrahmanyam, D. (2014). Solar x-ray monitor (xsm) on-board chandrayaan-2 orbiter. *Advances in Space Research*, 54(10):2021 – 2028. Lunar Science and Exploration.

Vadawale, S. V., Mithun, N. P. S., Mondal, B., Sarkar, A., Janardhan, P., Joshi, B., Bhardwaj, A., Shanmugam, M., Patel, A. R., Adalja, H. K. L., Goyal, S. K., Ladiya, T., Tiwari, N. K., Singh, N., and Kumar, S. (2021a). Observations of the quiet sun during the deepest solar minimum of the past century with chandrayaan-2 XSM: Sub-a-class microflares outside active regions. *The Astrophysical Journal Letters*, 912(1):L13.

Vadawale, S. V., Mondal, B., Mithun, N. P. S., Sarkar, A., Janardhan, P., Joshi, B., Bhardwaj, A., Shanmugam, M., Patel, A. R., Adalja, H. K. L., Goyal, S. K., Ladiya, T., Tiwari, N. K., Singh, N., and Kumar, S. (2021b). Observations of the quiet sun during the deepest solar minimum of the past century with chandrayaan-2 XSM: Elemental abundances in the quiescent corona. *The Astrophysical Journal Letters*, 912(1):L12.

Walker, A. B. C., J., Rugge, H. R., and Weiss, K. (1974). Relative Coronal Abundances Derived from X-Ray Observations. I. Sodium, Magnesium, Aluminum, Silicon, Sulfur, and Argon. *ApJ*, 188:423–440.

Widing, K. G. (1997). Emerging Active Regions on the Sun and the Photospheric Abundance of Neon. *ApJ*, 480(1):400–405.

Widing, K. G. and Feldman, U. (1993). Nonphotospheric abundances in a solar active region. *ApJ*, 416:392.

Widing, K. G. and Feldman, U. (2001). On the Rate of Abundance Modifications versus Time in Active Region Plasmas. *ApJ*, 555(1):426–434.

Winebarger, A. R., Warren, H. P., Schmelz, J. T., Cirtain, J., Mulu-Moore, F., Golub, L., and Kobayashi, K. (2012). Defining the "Blind Spot" of Hinode EIS and XRT Temperature Measurements. *ApJL*, 746(2):L17.

Young, P. R. and Mason, H. E. (1997). The Mg/Ne abundance ratio in a recently emerged flux region observed by CDS. *SoPh*, 175(2):523–539.